Research Square

Preprints are preliminary reports that have not undergone peer review.
They should not be considered conclusive, used to inform clinical practice,
or referenced by the media as validated information.

Quantitative in vivo imaging of intratumorally injected 125I-labeled nanoparticles using a benchtop 2D multi-pinhole X-ray system

Taeyun Kim
Seoul National University
Taewan Kim
Seoul National University
Hwijoon Jeong
Seoul National University
Byeongchan Lee
Korea Atomic Energy Research Institute
Jun Young Lee
Korea Atomic Energy Research Institute
Jeong Hoon Park
Korea Atomic Energy Research Institute
Sung-Joon Ye
sye@snu.ac.kr

Seoul National University https://orcid.org/0000-0001-8714-6317

Research Article

Keywords: Radiolabeled nanoparticles, iodine-125, cadmium zinc telluride detector, multi-pinhole collimator, intratumoral injection

Posted Date: July 25th, 2026

DOI: https://doi.org/10.21203/rs.3.rs-9310503/v1

License: This work is licensed under a Creative Commons Attribution 4.0 International License.
Read Full License

Quantitative in vivo imaging of intratumorally injected ^{125}I-labeled nanoparticles using a benchtop 2D multi-pinhole X-ray system

Taeyun Kim,[1,2] Taewan Kim,[1,3] Hwijoon Jeong,[1]
Byeongchan Lee,[3] Jun Young Lee,[3] Jeong Hoon Park,[3] Sung-Joon Ye,[1,2,4,5,6]

1. Department of Applied Bioengineering, Graduate School of Convergence Science and Technology, Seoul National University, Seoul, Republic of Korea
2. Research Institute, T-ROH Inc., Seoul, Republic of Korea
3. Cyclotron Application Research Section, Korea Atomic Energy Research Institute, Jeongeup, Republic of Korea
4. Research Institute for Convergence Science, Seoul National University, Seoul, Republic of Korea
5. Advanced Institute of Convergence Technology, Seoul National University, Suwon, Republic of Korea
6. Biomedical Research Institute, Seoul National University Hospital, Seoul, Republic of Korea

Corresponding author:
Sung-Joon Ye
Department of Applied Bioengineering
Graduate School of Convergence Science and Technology
Seoul National University
Seoul, 08826, Republic of Korea
Tel: +82-(2)-880-9560
Email: sye@snu.ac.kr

Running title: Preclinical in vivo imaging of ^{125}I-labeled nanoparticles

Manuscript Category: Original Article

Abstract

Purpose: Radiolabeled nanoparticles (NPs) are investigated for preclinical imaging and nano-brachytherapy, where accurate in vivo localization is essential. Here, we present a benchtop 2D multi-pinhole X-ray imaging system for characteristic X-ray imaging using an energy-resolving 2 × 2 cadmium zinc telluride detector.

Procedures: Polyethylene glycol (PEG)-coated iodine-125 (^{125}I)-labeled gold (Au) core and silver (Ag) shell NPs (hereafter ^{125}I-NPs) were used. The multi-pinhole X-ray imaging system was calibrated using ^{125}I-NPs containing solutions, and the detection limit was estimated. Three CT26 tumor-bearing BALB/c mice received intratumoral injections of 500 μCi ^{125}I-NPs. In vivo imaging was performed with 10-min scan times at 0, 3, 6, 24, 96, and 120 h post-injection, followed by endpoint ex vivo imaging of the excised tumor and major organs.

Results: The multi-pinhole X-ray imaging system showed linearity between activity and characteristic X-ray photon counts with R^2 = 0.9992, and the detection limit was 0.05 μCi. In vivo imaging quantified intratumoral retention kinetics, showing a marked decline within 24 h followed by a slower phase through 120 h. Endpoint ex vivo imaging supported high tumor selectivity at 120 h, with 26.41 ± 2.36% of the injected dose and 172.65 ± 15.45% of the injected dose per gram retained in the tumor. The liver and thyroid uptake remained low at 1.17 ± 0.90% of the injected dose and 0.77 ± 0.60% of the injected dose per gram in the liver and 1.92 ± 0.17% of the injected dose and 94.22 ± 8.15% of the injected dose per gram in the thyroid. The difference between in vivo and ex vivo measurements ranged from 0.03 to 3.51 μCi.

Conclusions: The multi-pinhole X-ray imaging system enables assessment of retention and biodistribution of ^{125}I-NPs, providing guidance for preclinical optimization when tumor retention and normal tissue safety are key design criteria.

Keywords: Radiolabeled nanoparticles, iodine-125, cadmium zinc telluride detector, multi-pinhole collimator, intratumoral injection

Introduction

Radiolabeled nanoparticles (NPs) have been extensively investigated for preclinical imaging and radionuclide-based therapy, including applications using gold nanoparticles (Au NPs) owing to their favorable chemistry and potential for multifunctional platforms [1–3]. In particular, iodine-125 (^{125}I)-labeled Au-based NPs have attracted attention in preclinical single-photon emission computed tomography (SPECT) imaging and in nano-brachytherapy, where accurate assessment of in vivo localization is essential for both efficacy and normal tissue safety [4–6]. However, systemic administration remains challenging for many NPs because substantial off-target accumulation in the reticuloendothelial system (RES), especially in the liver and spleen, can reduce effective tumor delivery and confound quantitative evaluation [7, 8]. In addition, deiodination and the consequent thyroid uptake can complicate the interpretation of radioiodinated tracers and may increase undesired exposure to radiosensitive tissue [9, 10].

For radiolabeled NPs, simultaneously achieving high intratumoral accumulation while minimizing uptake in normal organs is non-trivial, particularly when biodistribution is assessed only at a single time point [11, 12]. To address these challenges, intratumoral injection offers a direct route to maximize local delivery and to reduce systemic exposure compared with conventional intravenous injection, thereby providing a rational strategy for enhancing intratumoral retention [13–16]. In parallel, polyethylene glycol (PEG) coating is widely used as a surface modification intended to reduce protein adsorption and subsequent RES sequestration, which may further limit liver and spleen uptake [17–20]. Furthermore, a time-resolved understanding of retention and redistribution is important because early post-injection behavior can differ substantially from biodistribution at later time points [21].

From a translational standpoint, a practical preclinical workflow should support imaging at multiple time points to capture short-term pharmacokinetics and retention trends, while also enabling robust quantification across animals and organs [22]. While micro-SPECT provides sensitive imaging for radiolabeled NPs, it can be relatively resource-intensive and may not be accessible in all preclinical laboratories, motivating alternative imaging modalities for rapid screening of their biodistribution [23–25]. Complementary projection-based strategies (e.g., 2D imaging with a benchtop system) have therefore been explored for higher-throughput screening of NP kinetics and biodistribution in mice, particularly when reduced cost and operational simplicity are prioritized [26–29].

Here, we present a benchtop 2D multi-pinhole X-ray imaging system for detecting characteristic X-ray emissions associated with ^{125}I decay that leverages an energy-resolving High Energy X-ray Imaging Technology (HEXITEC) 2 × 2 cadmium zinc telluride (CZT) detector integrated with a

multi-pinhole collimator. To the best of our knowledge, this is the first in vivo demonstration of characteristic X-ray imaging of ^{125}I using the multi-pinhole X-ray imaging system equipped with a HEXITEC 2 × 2 CZT detector, and we extend its use to ex vivo evaluation. The objective of this study was to evaluate the time-dependent in vivo biodistribution of ^{125}I-labeled NPs following intratumoral injection in CT26 tumor-bearing BALB/c mice, validated by endpoint ex vivo imaging. This study further examined whether intratumoral injection provides sustained tumor retention with limited off-target uptake over 120 h.

Materials and Methods

Multi-Pinhole X-ray Imaging System

Figure 1 shows the multi-pinhole X-ray imaging system, which integrates the HEXITEC 2 × 2 CZT detector and the multi-pinhole collimator. The system consists of a stage for positioning the imaging object, the multi-pinhole collimator, and the HEXITEC 2 × 2 CZT detector coupled to a lead-shielded chamber. The HEXITEC detector can detect X-rays over an energy range of 4–200 keV and operates at room temperature [30]. The detector comprises four CZT modules; each module contains a 2-mm-thick CZT crystal with a planar platinum cathode and a pixelated platinum anode. The anode has an 80 × 80 pixel array with a 250 μm pixel pitch. The four modules are tiled in a 2 × 2 arrangement to form a 4 cm × 4 cm active area. The multi-pinhole collimator comprises four tungsten pinholes with inner and outer diameters of 2 and 4.88 mm, respectively; the remaining structure was made of lead with an overall thickness of 9 mm. The pinhole pitch was 1 cm. The detailed specifications and characteristics of the multi-pinhole X-ray imaging system have been described previously [31].

^{125}I-labeled metal nanoparticles were prepared at the Korea Atomic Energy Research Institute. They were polyethylene glycol (PEG)-coated iodine-125 (^{125}I)-labeled gold (Au) core and silver (Ag) shell NPs (hereafter ^{125}I-NPs). Its solutions with activities of 0.145, 0.289, 0.578, 1.16, 2.31, 4.63, 9.25, and 18.5 MBq (3.9, 7.8, 15.6, 31.3, 62.5, 125, 250, and 500 μCi) were used to establish a calibration curve relating activity to K-shell characteristic X-ray photon counts. A polymethyl methacrylate (PMMA) phantom with a height of 1.5 cm and a diameter of 1 cm was used for each activity. At the center, a cylindrical hole with a height of 1 cm and a diameter of 0.8 cm was filled with 500 μL of ^{125}I-NPs containing solution. The scan time for each measurement was 10 min. In addition, the ^{125}I-NP-loaded phantom filled with these solutions was used to evaluate the detection limit of the multi-pinhole X-ray imaging system. All measurements were corrected for radioactive decay.

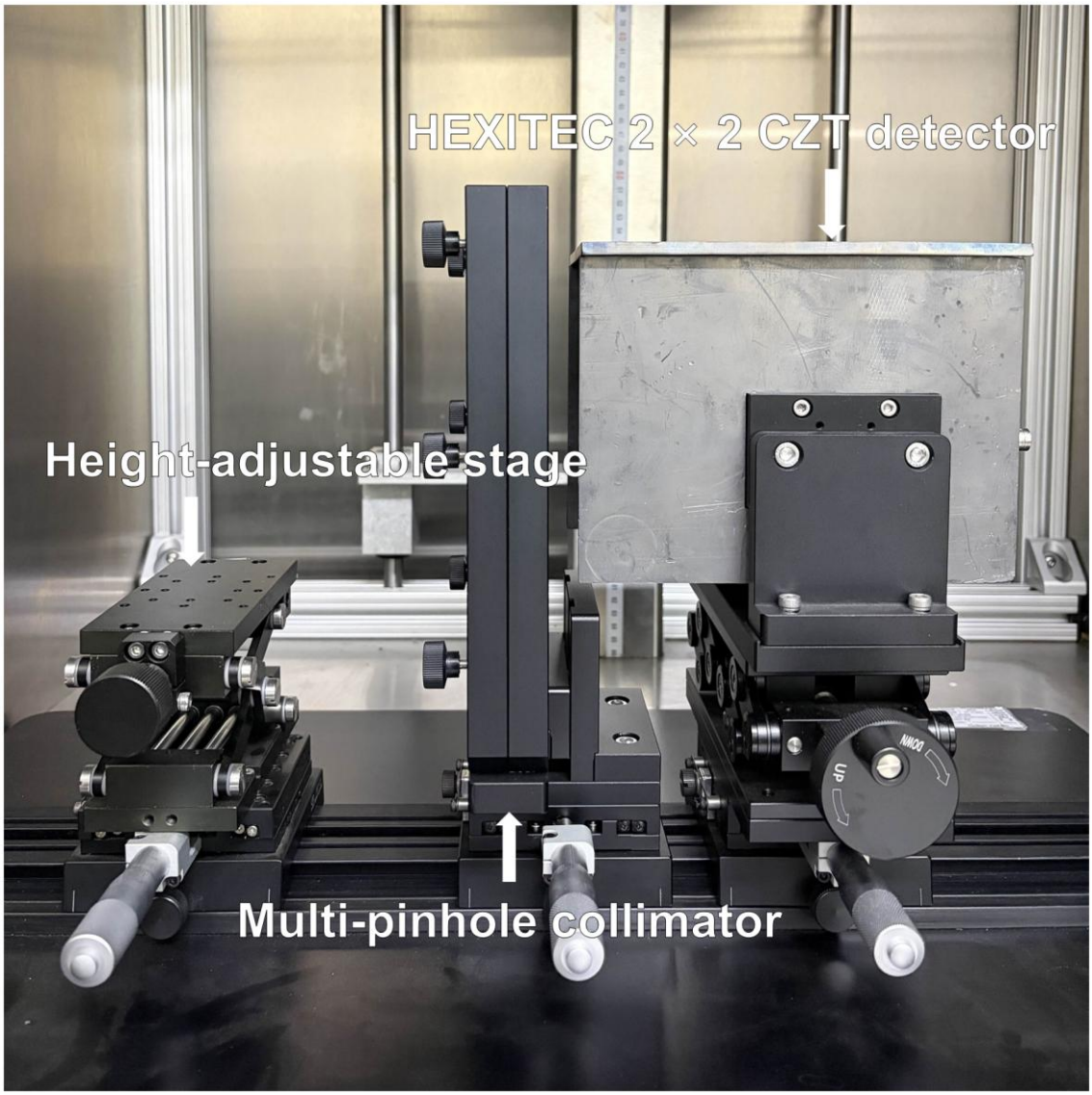


Figure 1. Multi-pinhole X-ray imaging system, which integrates the HEXITEC 2 × 2 CZT detector and the multi-pinhole collimator.

Image Processing and Analysis

The K_α characteristic X-ray peak at 27.5 keV from ^{125}I decay was extracted using the 26–29 keV energy window. Within this window, the peak and continuum background were modeled using Gaussian and linear functions, respectively, and the background was subtracted to obtain the K-shell characteristic X-ray photon counts. Image processing was performed on each detector pixel to generate projection images. After continuum background subtraction, a pixel-by-pixel nonuniformity correction was performed using a uniform photon field obtained from the 59.5 keV

photopeak of americium-241. The projection images were reconstructed using the maximum likelihood expectation maximization algorithm. Details of the pixel-by-pixel nonuniformity correction and reconstruction procedures have been described previously [31]. A pixel binning factor of 2 was applied by merging 2 × 2 pixels to improve counting statistics. Bicubic interpolation was applied to the reconstructed X-ray image for visualization. All image processing and reconstruction were implemented in MATLAB (R2023a, MathWorks Inc., Natick, MA, USA).

The contrast-to-noise ratio (CNR) was used to evaluate the reconstructed X-ray images. The CNR was calculated as the ratio of the difference in the average photon counts between the region of interest (ROI) and the background region to the standard deviation of the photon counts in the background region:

$$CNR = \frac{\overline{C}_{ROI} - \overline{C}_{BG}}{\sigma_{BG}} \qquad (1)$$

where $\overline{C}_{ROI}$ and $\overline{C}_{BG}$ are the average photon counts in the ROI and in the background region, respectively. σ_{BG} is the standard deviation of the photon counts in the background region. The ROI was defined in the center of the PMMA phantom, corresponding to the cylindrical hole filled with the ^{125}I-NPs-containing solution. The background region was defined as the region within the PMMA phantom surrounding the cylindrical hole, where no ^{125}I-NPs were present. According to the Rose criterion, a CNR of 5 was chosen to determine the detection limit [32]. Therefore, ^{125}I-NPs were considered undetectable in the reconstructed X-ray images when the CNR was less than 5.

Animal Study

Three 6-week-old female BALB/c mice with CT26 tumors were used. After cancer cell inoculation, the tumors were allowed to grow for 7 days. All animal experiments were conducted after confirming the absence of abnormal conditions. The mice were anesthetized with isoflurane gas via inhalation and positioned on a horizontal bed. Subsequently, ^{125}I-NPs were suspended in 50 μL of phosphate-buffered saline with an activity of 500 μCi and intratumorally injected into each CT26 tumor. The reconstructed X-ray images were obtained using the K-shell characteristic X-ray photon counts, and image processing was performed as described in the Image processing and analysis section. In vivo imaging was performed at 0, 3, 6, 24, 96, and 120 h post-injection, with a scan time of 10 min. The mice were euthanized by CO_2 inhalation after in vivo imaging. The tumor, liver, spleen, thyroid, and both kidneys were excised from each mouse and imaged ex vivo using the multi-pinhole X-ray imaging system for 10 min without sample preparation. The

measured activity of each organ was normalized to the injected activity to calculate the percentage of injected dose (%ID). The %ID was then normalized by organ weight to calculate the percentage of injected dose per gram of organ (%ID/g). All animal experiments were approved by the Institutional Animal Care and Use Committee of the Korea Atomic Energy Research Institute (Approval No. KAERI-IACUC-2024-001).

Results

Multi-Pinhole X-ray Imaging System

Figure 2a shows the photon spectrum of the ^{125}I-NPs-loaded phantom filled with a solution containing an activity of 500 μCi, with a 10-min scan time. The spectrum was extracted from the central pixel of the ^{125}I-NPs-loaded region. In the photon spectrum, the K_α characteristic X-ray peak at 27.5 keV from ^{125}I decay was observed. Figure 2b shows the calibration curve of the multi-pinhole X-ray imaging system relating activity to K-shell characteristic X-ray photon counts. The black dashed line represents the linear regression line between activity and K-shell characteristic X-ray photon counts, indicating a strong linear relationship (R^2 = 0.9992).

Figure 2c shows the CNR as a function of activity in the reconstructed X-ray images (Fig. 2d). The CNRs at activities of 3.9 and 500 μCi were 91.50 ± 9.64 and 9317.41 ± 263.58, respectively. According to the Rose criterion (CNR > 5), the multi-pinhole X-ray imaging system was able to detect ^{125}I-NPs at an activity of 3.9 μCi. The black dashed line represents the linear regression line between activity and CNR, indicating a strong linear relationship (R^2 = 0.9985). This regression line was used to estimate the activity corresponding to a CNR of 5, which defined the detection limit of the multi-pinhole X-ray imaging system. The estimated detection limit was 0.05 μCi. Figure 2d shows the reconstructed X-ray images of the ^{125}I-NPs-loaded phantom filled with solutions containing 3.9–500 μCi of activity. With decreasing activity, the ^{125}I-NPs-loaded region showed increased noise, while its location remained unchanged.

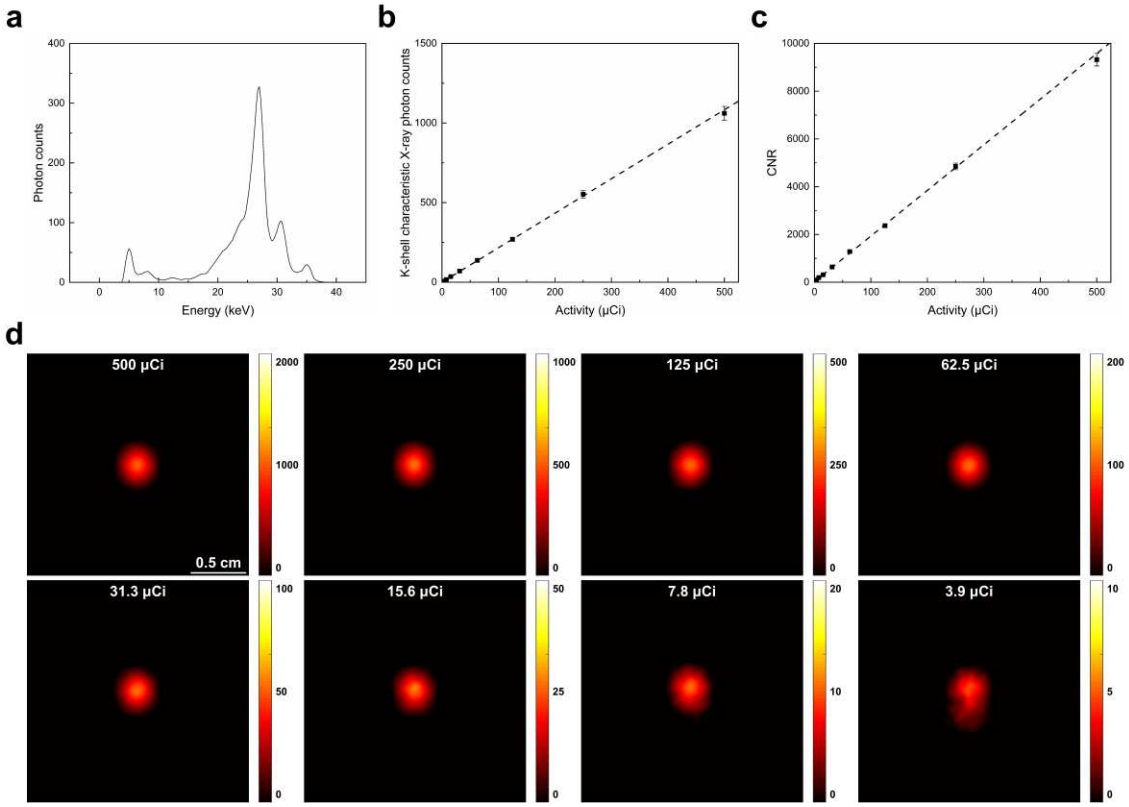


Figure 2. (a) Photon spectrum of the ^{125}I-NPs-loaded phantom filled with a solution containing an activity of 500 μCi, with a 10-min scan time. (b) Calibration curve of the multi-pinhole X-ray imaging system relating activity to K-shell characteristic X-ray photon counts. Error bars represent the 95% confidence intervals, but some are smaller than the marker size. (c) CNR as a function of activity in the reconstructed X-ray images. Error bars represent the 95% confidence intervals, but some are smaller than the marker size. (d) Reconstructed X-ray images of the ^{125}I-NPs-loaded phantom filled with solutions containing 3.9–500 μCi of activity. The color bars indicate the K-shell characteristic X-ray photon counts.

Animal study

Figure 3 shows the photographs and in vivo reconstructed X-ray images of mouse 1 (M1), mouse 2 (M2), and mouse 3 (M3) at 0, 3, 6, 24, 96, and 120 h post-injection. The tumor, liver, and thyroid were clearly identified in the in vivo reconstructed X-ray images. Due to the intratumoral injection of ^{125}I-NPs, the tumor and liver showed the highest uptake immediately after injection. As time elapsed, ^{125}I-NPs were progressively cleared from the tumor and liver. The thyroid became more clearly identifiable at T = 3 h.

Figure 4 shows the time-activity curves (TACs) of ^{125}I-NPs in the tumor, liver, and thyroid of M1, M2, and M3. To quantify the average activity in the in vivo reconstructed X-ray images, ROIs were selected as 8 × 8 pixels in the tumor, liver, and thyroid. The TACs for the tumor showed that ^{125}I-NPs were rapidly cleared by T = 24 h, followed by a slower decline thereafter. At T = 120 h, activity in the tumor was similar across all three mice. M2 exhibited faster clearance from the tumor than M1 and M3, and this was accompanied by a slightly higher early uptake of ^{125}I-NPs in the liver. The TACs for the liver showed that activity in the liver decreased gradually over time in all three mice. In contrast, the TACs for the thyroid showed lower uptake than the tumor and liver, but they showed an early increase and then remained relatively stable through 120 h. M2 consistently exhibited slightly higher activity in the thyroid than M1 and M3, similar to the liver.

Figure 5 shows the photographs and ex vivo reconstructed X-ray images of the excised tumor and organs from M1, M2, and M3. Consistent with the in vivo reconstructed X-ray images at T = 120 h, uptake of ^{125}I-NPs was clearly identified in the tumor and thyroid in all three mice, while the liver showed relatively low uptake. In contrast, uptake in the spleen and kidneys was indistinguishable from background, indicating negligible uptake of ^{125}I-NPs.

Figure 6a–c show the in vivo and ex vivo activity in the excised tumor and organs of M1, M2, and M3. Across the excised tumor and organs, the difference between in vivo and ex vivo measurements ranged from 0.03 to 3.51 μCi. In the tumor, the in vivo activity was 146.73 ± 8.53, 122.61 ± 7.75, and 123.69 ± 7.42 μCi for M1, M2, and M3, respectively, whereas the corresponding ex vivo activity was 144.06 ± 7.27, 124.96 ± 5.12, and 127.20 ± 6.68 μCi. In the liver, the in vivo activity was 3.27 ± 1.79, 9.14 ± 2.27, and 4.02 ± 2.12 μCi, respectively, whereas the ex vivo activity was 3.04 ± 1.29, 10.39 ± 2.23, and 4.05 ± 1.45 μCi. In the thyroid, the in vivo activity was 9.88 ± 3.07, 10.30 ± 2.36, and 8.64 ± 2.04 μCi, respectively, whereas the ex vivo activity was 10.39 ± 2.80, 9.37 ± 2.95, and 8.98 ± 2.86 μCi. Figure 6d,e show the average %ID and %ID/g across all three mice. The average %ID in the tumor, liver, and thyroid was 26.41 ± 2.36, 1.17 ± 0.90, and 1.92 ± 0.17, respectively. The average %ID/g in the tumor, liver, and thyroid was 172.65 ± 15.45, 0.77 ± 0.60, and 94.22 ± 8.15, respectively.

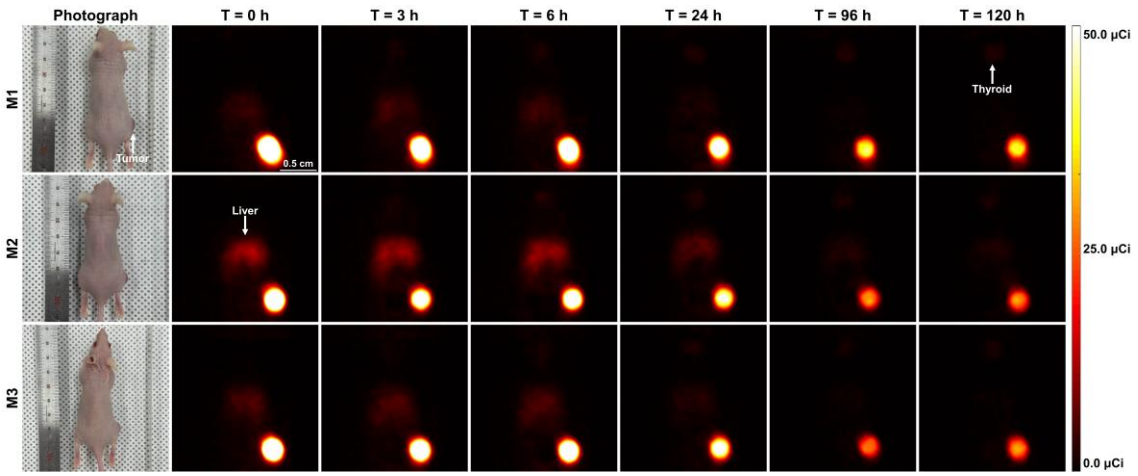


Figure 3. Photographs and in vivo reconstructed X-ray images of M1, M2, and M3 at 0, 3, 6, 24, 96, and 120 h post-injection. The color bar indicates the activity.

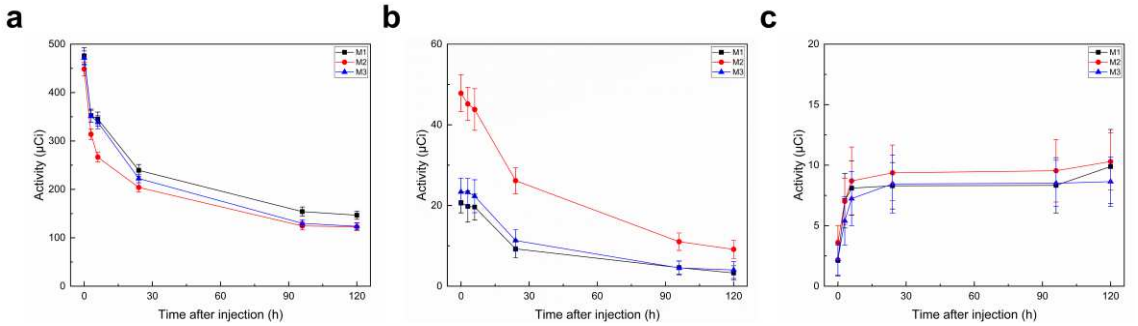


Figure 4. TACs of ^{125}I-NPs in the (a) tumor, (b) liver, and (c) thyroid of M1, M2, and M3. Error bars represent the 95% confidence intervals.

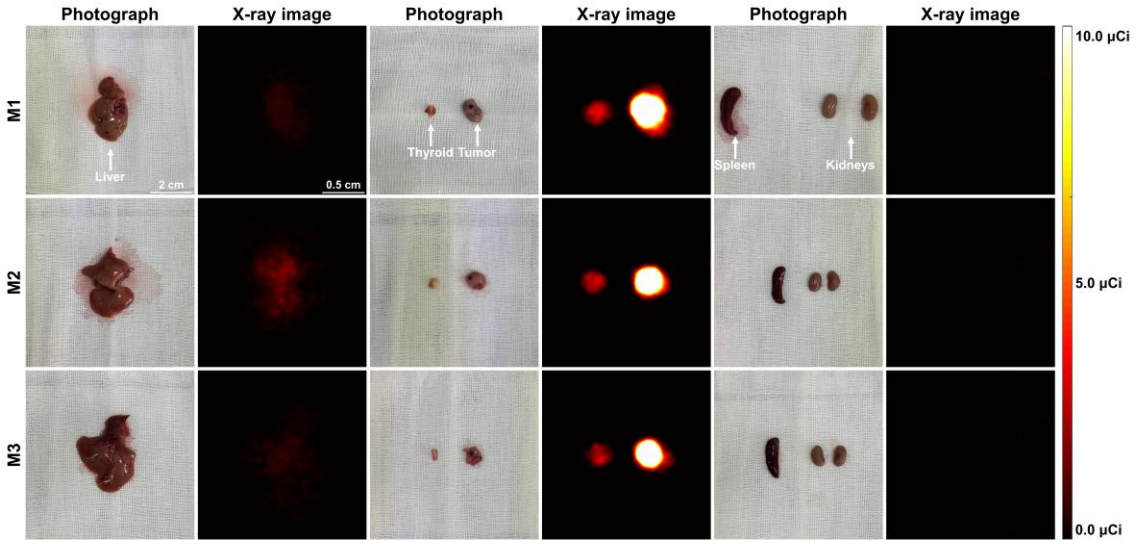


Figure 5. Photographs and ex vivo reconstructed X-ray images of the excised tumor and organs from M1, M2, and M3. The color bar indicates the activity.

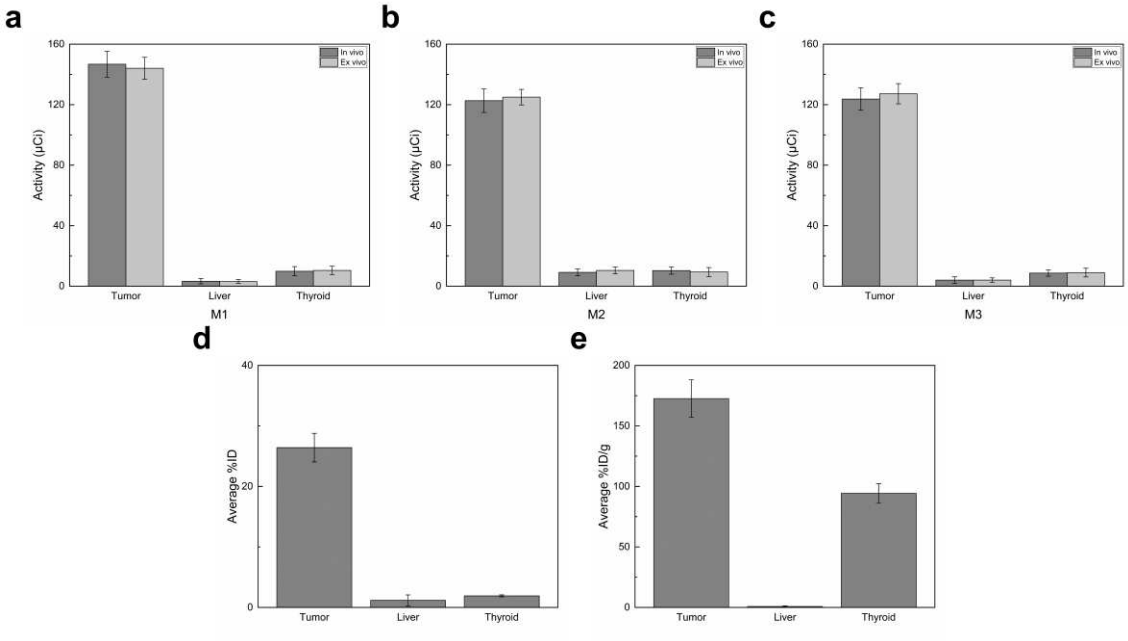


Figure 6. In vivo and ex vivo activity in the excised tumor and organs of (a) M1, (b) M2, and (c) M3. Average (d) %ID and (e) %ID/g across all three mice. Error bars represent the 95% confidence intervals.

Discussion

^{125}I-NPs remained highly localized within the tumor for 120 h after intratumoral injection, while maintaining a comparatively low uptake in major off-target organs over the same period. Rather than relying on a single time point biodistribution measurement, imaging at multiple time points allowed the evaluation of the retention kinetics of ^{125}I-NPs [33]. The tumor uptake exhibited a marked early decline within 24 h, followed by a slower phase that persisted through 120 h, which was consistent with an initial loss from the injection site (e.g., redistribution within the tumor, drainage through lymphatics, or vascular leakage) and a longer-lived fraction retained within the tumor microenvironment [34]. Importantly, at T = 120 h, the biodistribution of ^{125}I-NPs showed high tumor selectivity; the tumor retained approximately 26 %ID at T = 120 h, whereas the liver and thyroid remained at approximately 1–2 %ID. Consistently, when normalized by organ weight, the tumor also showed a high uptake of approximately 173 %ID/g, whereas the liver remained low at less than 1 %ID/g. The absence of discernible uptake above background in the spleen and

kidneys at T = 120 h further supported the notion that systemic exposure was limited at late time points and that the residual activity was not widely redistributed to RES organs [35].

It should be noted that our imaging evaluated the biodistribution of the radioiodine label on the ^{125}I-NPs, rather than directly measuring the NPs themselves, and thus reflected in vivo biodistribution of NPs only to the extent that the ^{125}I label remained associated with the ^{125}I-NPs. The early liver uptake, which was highest at the earliest time point and declined thereafter, was suggestive of transient leakage into circulation followed by clearance rather than predominant RES trapping [36]. Consistent with this interpretation, the low late-time liver and spleen uptake suggested limited RES sequestration, which is in line with the PEG coating reducing protein adsorption and macrophage uptake [18]. From the standpoint of radioiodinated NPs, thyroid uptake is commonly monitored as an indicator of in vivo deiodination [37]. In this study, activity in the thyroid remained low in terms of %ID, with approximately 2 %ID at T = 120 h. By contrast, %ID/g was approximately 94 %ID/g, which is expected given the small thyroid weight. Notably, the thyroid TAC showed an early increase and was largely maintained thereafter, which is consistent with limited deiodination of the radioiodine label on the ^{125}I-NPs [38]. Imaging at multiple time points demonstrated quantitatively that ^{125}I-NPs exhibited strong intratumoral retention with minimal late-time redistribution to RES organs and a modest thyroid %ID, supporting their suitability for applications in which tumor retention and normal tissue safety are key design criteria [39].

The benchtop 2D multi-pinhole X-ray imaging system could be used not only for in vivo imaging of ^{125}I-NPs but also for quantitative biodistribution evaluation, validated against ex vivo measurements obtained on the same system. In preclinical imaging workflows, such as SPECT, robust quantification is often tied to fully tomographic acquisition and reconstruction [40]. However, tomographic systems impose cost, infrastructure, and operational complexity that can limit throughput and accessibility [41]. In this context, our study supported the feasibility of quantitative evaluation with the 2D imaging system by combining multiple time points in vivo imaging to generate TACs in the same animals and an in vivo and ex vivo comparison at an endpoint. This reduced inter-animal variability and allowed interpretation to focus on trends such as early and late change rather than only at a single time point, while enabling a consistency assessment that is often not readily available when ex vivo quantification is performed with a different modality (e.g., gamma counter) and different geometries [42]. This 2D imaging system is not a replacement for full tomographic reconstruction when 3D localization is essential, but the small in vivo and ex vivo differences supported the use of the 2D imaging system as a practical alternative for rapid,

repeated measurements of retention and redistribution across time [43]. It also demonstrated a reproducible workflow in which noninvasive in vivo evaluation and endpoint ex vivo validation are coupled.

A common limitation of intravenous injection studies is that systemic administration is typically inefficient for tumor accumulation, with a substantial fraction of injected NPs accumulating in RES organs and only a small fraction remaining in the tumor. Reported tumor accumulation after intravenous injection is typically less than 1 %ID, with dominant RES uptake [44]. In an intravenous injection study using ^{125}I-labeled Ag NPs, activity in RES organs was substantial, with approximately 25 %ID/g in the liver and approximately 42 %ID/g in the spleen at T = 24 h [45]. By contrast, in this study, intratumoral injection resulted in liver activity of less than 1 %ID/g at T = 120 h, likely reflecting the combined effects of administration route and the PEG-mediated stealth effect in reducing RES uptake. Against this background, ^{125}I-NPs retained approximately 26 %ID in the tumor at T = 120 h after intratumoral injection, highlighting the impact of administration route on achieving high intratumoral accumulation rather than competing with RES uptake for systemic delivery. The tumor retained approximately 26 %ID at T = 120 h, while liver and thyroid remained at approximately 1–2 %ID, supporting a high tumor-to-normal-organ contrast for the ^{125}I-NPs. This distinction is relevant to the nano-brachytherapy rationale, because therapeutic efficacy in this setting is driven primarily by intratumoral residence time and early leakage kinetics rather than by incremental improvements in intravenous targeting efficiency [46]. It should be noted that direct quantitative comparisons with intravenous injection studies are not always straightforward because reporting metrics and time points often differ. Nevertheless, at T = 120 h, the high tumor retention with low late-time off-target uptake supported the advantage of intratumoral injection in maintaining the localization of ^{125}I-NPs. Future work should include a matched intravenous injection group using the same ^{125}I-NPs. This would improve the ability to separate effects on tumor retention and off-target uptake. In addition, quantification relied on characteristic X-ray emissions associated with ^{125}I decay as a surrogate for the in vivo biodistribution of NPs; although endpoint ex vivo measurements on the same system supported consistency, complementary methods such as inductively coupled plasma mass spectrometry would further strengthen interpretation by directly quantifying the ^{125}I-NPs.

Conclusions

This study demonstrated the feasibility of the benchtop multi-pinhole X-ray imaging system for quantitative in vivo imaging of intratumorally injected ^{125}I-NPs at multiple time points in CT26 tumor-bearing BALB/c mice. To the best of our knowledge, this study provides the first in vivo

demonstration of characteristic X-ray imaging of ^{125}I using a multi-pinhole X-ray imaging system equipped with the HEXITEC 2 × 2 CZT detector, and it further extends the approach to ex vivo evaluation. The multi-pinhole X-ray imaging system showed a strong linear relationship between activity and K-shell characteristic X-ray photon counts, and the estimated detection limit was 0.05 μCi. In vivo imaging at multiple time points up to T = 120 h quantified intratumoral retention kinetics in the same animals, showing a marked early decline within 24 h followed by a slower phase through 120 h. Endpoint ex vivo imaging supported high tumor retention at T = 120 h, with 26.41 ± 2.36 %ID and 172.65 ± 15.45 %ID/g retained in the tumor. Agreement between in vivo and ex vivo measurements, with differences ranging from 0.03 to 3.51 μCi across organs, supported the quantitative reliability of the system. Overall, the multi-pinhole X-ray imaging system enables rapid, repeated quantitative assessment of intratumoral retention and biodistribution of ^{125}I-NPs, providing a practical preclinical imaging workflow when intratumoral residence time and normal tissue safety are key design criteria.

Author Contributions: TYK and SJY designed the study. TYK, TWK, and HJ acquired the experimental data. TWK established the animal model. BL, JYL, and JHP prepared the nanoparticles. TYK drafted the manuscript. TWK, HJ, BL, JYL, JHP, and SJY revised the manuscript. All authors read and approved the final manuscript.

Acknowledgements: Not applicable.

Funding: This work was supported by a National Research Foundation of Korea (NRF) grant funded by the Korea government (MSIT) (RS-2023-00237149) and by Basic Science Research Program through the National Research Foundation of Korea (NRF) funded by the Ministry of Education (2022R1A6A1A03063039).

Conflicts of Interest: The authors declare that they have no conflict of interest with regard to this study.

Ethical Approval: This study followed all applicable institutional and/or national guidelines for the care and use of animals.

Data Availability: All research data and computer codes are available from the corresponding author upon request.

References

1. Pellico J, Gawne PJ, de Rosales RTM (2021) Radiolabelling of nanomaterials for medical imaging and therapy. Chem Soc Rev 50:3355–3423
2. Pijeira MSO, Viltres H, Kozempel J, et al. (2022) Radiolabeled nanomaterials for biomedical applications: Radiopharmacy in the era of nanotechnology. EJNMMI Radiopharm Chem 7:8
3. Daems N, Michiels C, Lucas S, Baatout S, Aerts A (2021) Gold nanoparticles meet medical radionuclides. Nucl Med Biol 100–101:61–90
4. Kim YH, Jeon J, Hong SH, et al. (2011) Tumor targeting and imaging using cyclic RGD-PEGylated gold nanoparticle probes with directly conjugated iodine-125. Small 7:2052–2060
5. Shao X, Zhang H, Rajian JR, et al. (2011) ^{125}I-labeled gold nanorods for targeted imaging of inflammation. ACS Nano 5:8967–8973
6. Seniwal B, Thipe VC, Singh S, Fonseca TCF, Freitas de Freitas L (2021) Recent advances in brachytherapy using radioactive nanoparticles: An alternative to seed-based brachytherapy. Front Oncol 11:766407
7. Wilhelm S, Tavares AJ, Dai Q, et al. (2016) Analysis of nanoparticle delivery to tumours. Nat Rev Mater 1:16014
8. Li SD, Huang L (2009) Nanoparticles evading the reticuloendothelial system: Role of the supported bilayer. Biochim Biophys Acta Biomembr 1788:2259–2266
9. Cavina L, van der Born D, Klaren PHM, et al. (2017) Design of radioiodinated pharmaceuticals: Structural features affecting metabolic stability towards in vivo deiodination. Eur J Org Chem 2017:3387–3414
10. Mushtaq S, Nam YR, Kang JA, Choi DS, Park SH (2018) Efficient and site-specific ^{125}I-radioiodination of bioactive molecules using oxidative condensation reaction. ACS Omega 3:6903–6911
11. Drozdov AS, Nikitin PI, Rozenberg JM (2021) Systematic review of cancer targeting by nanoparticles revealed a global association between accumulation in tumors and spleen. Int J Mol Sci 22:13011

12. Kadam RS, Bourne DWA, Kompella UB (2012) Nano-advantage in enhanced drug delivery with biodegradable nanoparticles: Contribution of reduced clearance. Drug Metab Dispos 40:1380–1388

13. Holback H, Yeo Y (2011) Intratumoral drug delivery with nanoparticulate carriers. Pharm Res 28:1819–1830

14. Jiang Z, Fu Y, Shen H (2024) Development of intratumoral drug delivery based strategies for antitumor therapy. Drug Des Devel Ther 18:2189–2202

15. Xie H, Goins B, Bao A, Wang ZJ, Phillips WT (2012) Effect of intratumoral administration on biodistribution of ^{64}Cu-labeled nanoshells. Int J Nanomed 7:2227–2238

16. Yook S, Cai Z, Lu Y, et al. (2016) Intratumorally injected ^{177}Lu-labeled gold nanoparticles: Gold nanoseed brachytherapy with application for neoadjuvant treatment of locally advanced breast cancer. J Nucl Med 57:936–942

17. Suk JS, Xu Q, Kim N, Hanes J, Ensign LM (2016) PEGylation as a strategy for improving nanoparticle-based drug and gene delivery. Adv Drug Deliv Rev 99:28–51

18. Shi L, Zhang J, Zhao M, et al. (2021) Effects of polyethylene glycol on the surface of nanoparticles for targeted drug delivery. Nanoscale 13:10748–10764

19. Amoozgar Z, Yeo Y (2012) Recent advances in stealth coating of nanoparticle drug delivery systems. Wiley Interdiscip Rev Nanomed Nanobiotechnol 4:219–233

20. Peracchia MT, Fattal E, Desmaële D, et al. (1999) Stealth® PEGylated polycyanoacrylate nanoparticles for intravenous administration and splenic targeting. J Control Release 60:121–128

21. Ding H, Wu F (2012) Image guided biodistribution and pharmacokinetic studies of theranostics. Theranostics 2:1040–1053

22. Arms L, Smith DW, Flynn J, et al. (2018) Advantages and limitations of current techniques for analyzing the biodistribution of nanoparticles. Front Pharmacol 9:802

23. Vanhove C, Koole M, Fragoso Costa P, et al. (2024) Preclinical SPECT and PET: Joint EANM and ESMI procedure guideline for implementing an efficient quality control programme. Eur J Nucl Med Mol Imaging 51:3822–3839

24. Lall R, Lee K, Chopra S, et al. (2024) Low cost, high temporal resolution optical fiber-

based γ-photon sensor for real-time pre-clinical evaluation of cancer-targeting radiopharmaceuticals. Biosens Bioelectron 247:115956

25. Desmonts C, Aide N, Austins H, Jaudet C, Lasnon C (2022) Feasibility of imaging small animals on a 360° whole-body cadmium zinc telluride SPECT camera: A phantom study. Mol Imaging Biol 24:1018–1027

26. Yagishita A, Takeda S, Katsuragawa M, et al. (2022) Simultaneous visualization of multiple radionuclides in vivo. Nat Biomed Eng 6:640–647

27. Rouchota M, Adamiano A, Iafisco M, et al. (2021) Optimization of in vivo studies by combining planar dynamic and tomographic imaging: Workflow evaluation on a superparamagnetic nanoparticles system. Mol Imaging 2021:6677847

28. Georgiou M, Fysikopoulos E, Mikropoulos K, Fragogeorgi E, Loudos G (2017) Characterization of “γ-eye”: A low-cost benchtop mouse-sized gamma camera for dynamic and static imaging studies. Mol Imaging Biol 19:398–407

29. Fysikopoulos E, Rouchota M, Georgiou M, et al. (2022) β-eye: A benchtop system for in vivo molecular screening of labeled compounds. Appl Radiat Isot 180:110034

30. Veale MC, Seller P, Wilson M, Liotti E (2018) HEXITEC: A high-energy X-ray spectroscopic imaging detector for synchrotron applications. Synchrotron Radiat News 31:28–32

31. Kim T, Eom M, Wilson MD, et al. (2026) Benchtop 2D multi-pinhole X-ray fluorescence imaging system using a high energy resolution pixelated cadmium zinc telluride detector. Med Phys 53:e70265

32. Cherry SR, Sorenson JA, Phelps ME Physics in nuclear medicine, 3rd edn. Saunders, Philadelphia

33. Carter LM, Zanzonico PB (2024) MIB Guides: Preclinical radiopharmaceutical dosimetry. Mol Imaging Biol 26:17–28

34. Kim J, Song S, Gwak M, et al. (2023) Micro-syringe chip-guided intratumoral administration of lipid nanoparticles for targeted anticancer therapy. Biomater Res 27:102

35. Yun WS, Kim J, Lim DK, et al. (2023) Recent studies and progress in the intratumoral administration of nano-sized drug delivery systems. Nanomaterials 13:2225

36. Seo HJ, Nam SH, Im HJ, et al. (2015) Rapid hepatobiliary excretion of micelle-encapsulated/radiolabeled upconverting nanoparticles as an integrated form. Sci Rep 5:15685

37. Läppchen T, Tönnesmann R, Eersels J, et al. (2017) Radioiodinated exendin-4 is superior to the radiometal-labelled glucagon-like peptide-1 receptor probes overcoming their high kidney uptake. PLoS One 12:e0170435

38. Nurhidayah W, Setyawati LU, Daruwati I, et al. (2022) Future prospective of radiopharmaceuticals from natural compounds using iodine radioisotopes as theranostic agents. Molecules 27:8009

39. Zhang S, Wang X, Gao X, et al. (2025) Radiopharmaceuticals and their applications in medicine. Signal Transduct Target Ther 10:1

40. Wright JD, Renard I, Middleton IA, et al. (2025) Quantitative whole-body dynamic planar scintigraphy in mice with ^{99m}Tc and ^{161}Tb. EJNMMI Phys 12:61

41. Fysikopoulos E, Rouchota M, Eleftheriadis V, et al. (2021) Optical to planar X-ray mouse image mapping in preclinical nuclear medicine using conditional adversarial networks. J Imaging 7:262

42. Imlimthan S, Berton C, Poty S, Holland JP, Sarparanta M (2025) A guide to ex vivo biodistribution studies with radiotracers in rodent models. Mol Imaging Biol 27:883–893

43. Dietze MMA, de Jong HWAM (2022) Progress in large field-of-view interventional planar scintigraphy and SPECT imaging. Expert Rev Med Devices 19:393–403

44. Chen Q, Yuan L, Chou WC, et al. (2023) Meta-analysis of nanoparticle distribution in tumors and major organs in tumor-bearing mice. ACS Nano 17:19810–19831

45. Chrastina A, Schnitzer JE (2010) Iodine-125 radiolabeling of silver nanoparticles for in vivo SPECT imaging. Int J Nanomed 5:653–659

46. Momin N, Palmeri JR, Lutz EA, et al. (2022) Maximizing response to intratumoral immunotherapy in mice by tuning local retention. Nat Commun 13:109

Supplementary Files

This is a list of supplementary files associated with this preprint. Click to download.

- ManuscriptI125HEXITECCOIMIBByeongchanLee260402.pdf
- ManuscriptI125HEXITECCOIMIBHwijoonJeong260402.pdf
- ManuscriptI125HEXITECCOIMIBJeongHoonPark260402.pdf
- ManuscriptI125HEXITECCOIMIBJunYoungLee260402.pdf
- ManuscriptI125HEXITECCOIMIBSungJoonYe260402.pdf
- ManuscriptI125HEXITECCOIMIBTaewanKim260402.pdf
- ManuscriptI125HEXITECCOIMIBTaeyunKim260402.pdf